Invited paper

OPTO-ELECTRONICS REVIEW **10**(4), 251–260 (2002)

UV detectors and focal plane array imagers based on AlGaN p-i-n photodiodes

J.P. LONG, S. VARADARAAJAN, J. MATTHEWS, and J.F. SCHETZINA*

Department of Electrical and Computer Engineering, North Carolina State University, Raleigh, NC 27695, USA

The successful development of both discrete UV photodiodes and large-format UV imaging arrays consisting of 128×128 and 320×256 AlGaN p-i-n photodiodes is reported. Detectors and detector arrays have been successfully developed to sense radiation in the 300–365 nm visible-blind and 240–285 nm solar-blind portions of the UV spectral region. Details of the device synthesis and processing are discussed, including flip-chip bonding procedures employed to mate the UV photodiode arrays to silicon read-out integrated circuits (ROICs). A selection of UV images obtained using these new large-format UV digital imagers is included.

Keywords: UV detector, UV focal plane array, UV digital camera.

1. Introduction

The development of semiconductor photodetectors covering the visible and infrared (IR) spectral regions has lead to the development of large format digital imagers. In the far-IR (8–14 μm wavelength region), HgCdZnTe has become the material of choice and is now used in a wide variety of night vision applications including far IR digital imagery. In the mid-IR (2–5 μm wavelength region), InSb is the material of choice. Digital cameras that employ large-format (320×256 pixel) InSb focal plane arrays (FPAs) have been developed and are available commercially [1] for use in a number of applications including military surveillance, medical imagery, crime scene analysis, forensic investigations, and defect analysis. In the 0.9–1.68 μm near-IR region, highly sensitive FPAs based on InGaAs have been developed for similar applications.

In addition, over the past ten years there has been a revolution in digital imagery in the visible wavelength region based on the development of very large arrays of Si charge-coupled devices (CCDs), and Si imagers based on complimentary metal-oxide semiconductor (CMOS) circuitry. Very large format (greater than five million pixel) digital cameras based on Si CCDs are now widely available commercially at reasonable prices. These new digital cameras represent a viable alternative to traditional 35-mm film photography.

Until recently, however, there has been no semiconductor material under development for UV-specific detector applications. Atmospheric absorption of sunlight by ozone and oxygen gives rise to a narrow UV absorption band at the earth's surface from about 240–285 nm that is termed the 'solar-blind' UV region [2,3]. UV detectors that respond exclusively to radiation in this wavelength region are termed 'solar-blind' detectors since they can detect objects that emit radiation in this narrow wavelength window without interference from the sun - provided that both the detector and the object of interest are at or near the surface of the earth. Solar-blind detectors are to be distinguished from 'visible-blind' UV detectors and detector arrays that have UV responsivity bands outside of the solar-blind window but remain blind to visible radiation. Visible-blind UV detectors and detector arrays based on III-V nitride structures that have responsivity bands in the 300–365 nm region have been reported in a number of recent publications [3–11].

This paper reports the successful synthesis, fabrication, and testing of both visible-blind and solar-blind back-side-illuminated UV detectors based on AlGaN p-i-n heterostructures. The structure of these devices is first described. This is followed by a description of the experimental procedures employed to synthesise and characterise the various layers of the heterostructure. Processing procedures used to prepare discrete 200×200 μm mesa photodiodes are next described, followed by a discussion of the device characteristics obtained from spectral responsivity R_λ and R_0A measurements from which the photodiode detectivity D^* was estimated.

This paper also reports the successful development of large-format UV imaging arrays consisting of 128×128 and 320×256 AlGaN p-i-n photodiodes designed to sense radiation in the 300–365 nm and 250–285 nm portions of the UV spectral region. Details of the device synthesis and processing are discussed, including flip-chip bonding proce-

*e-mail: jan_schetzina@ncsu.edu

dures to silicon read-out integrated circuits (ROICs). A selection of UV images obtained using these new large-format UV digital cameras is also included.

2. Properties of semiconductor photodiodes

Let us consider a p-n junction or p-i-n junction photodiode operating in the photovoltaic mode at zero bias [12]. The detector current responsivity R_λ is defined as the output current i_p produced by the detector divided by the diode illumination power P_λ at a given wavelength λ. That is,

$$R_\lambda = i_p / P_\lambda = q\eta / h\nu \quad \text{(A/W)} \tag{1}$$

where q is the electronic charge, η is the quantum efficiency, h is the Planck's constant and ν is the radiation frequency. Note that the responsivity R_λ varies inversely with the optical frequency ν. As a consequence, the maximum responsivities ($\eta = 1$) in the UV are small - ranging from $R_\lambda = 0.294$ A/W at 365 nm to $R_\lambda = 0.161$ A/W at 200 nm.

An important figure of merit for a diode detector is the R_0A product, where R_0 is the dynamic resistance of the diode at zero bias and A is the detector area. A large R_0A product is a necessary requirement for the detector to have a large detectivity D^*. That is, for the detector to be able to detect very low light levels. Figure 1 shows the spectral detectivity D^* for a number of different commercially-available detectors [13] that operate at wavelengths ranging from 0.2 μm (UV) to 12 μm (IR). It is seen from the figure that IR detectors display D^* values of 10^7–10^{10} cmHz$^{1/2}$W^{-1} depending on the type of detector, its operating temperature, and the wavelength region for which it is designed. Detectors operating at shorter wavelengths generally display larger D^* values ranging up to $D^* = 4\times10^{14}$ cmHz$^{1/2}$W^{-1} for a photomultiplier tube (PMT) operating at about 300 nm.

Figure 1 also shows the curve for an ideal photovoltaic detector limited by thermal background radiation from a 293 K radiation source (the earth!!). A detector displaying D^* values that lie along this line is said to be background limited. A background limited photodetector is often referred to as being a BLIP-limited detector, or as being BLIP-limited [12]. These detectors have the highest possible D^* values for a given wavelength when exposed to the earth's thermal radiation field. Note from the figure, that D^* values for a BLIP-limited detector become extremely large as the wavelength decreases into the UV. This is because a 293 K black body radiation background contains virtually no UV radiation, so an extremely sensitive detector is required to be able to be detect this near-zero thermal background from the earth.

The spectral detectivity D^* of a photodiode detector may be expressed as [12]

$$D^* = (q\eta/h\nu)\left[(4kT/R_0A) + 2q^2\eta\Phi_b\right]^{-1/2} \quad (\text{cmHz}^{1/2}\text{W}^{-1}) \tag{2}$$

The first term in the bracketed quantity above $(4kT/R_0A)$ arises from thermal noise sources within the detector. The second term $(2q^2\eta\Phi_b)$ is due to the background radiation Φ_b to which the detector is exposed. If the detector is limited by thermal noise, that is, if the thermal noise far exceeds the background radiation induced signal, then the detectivity becomes

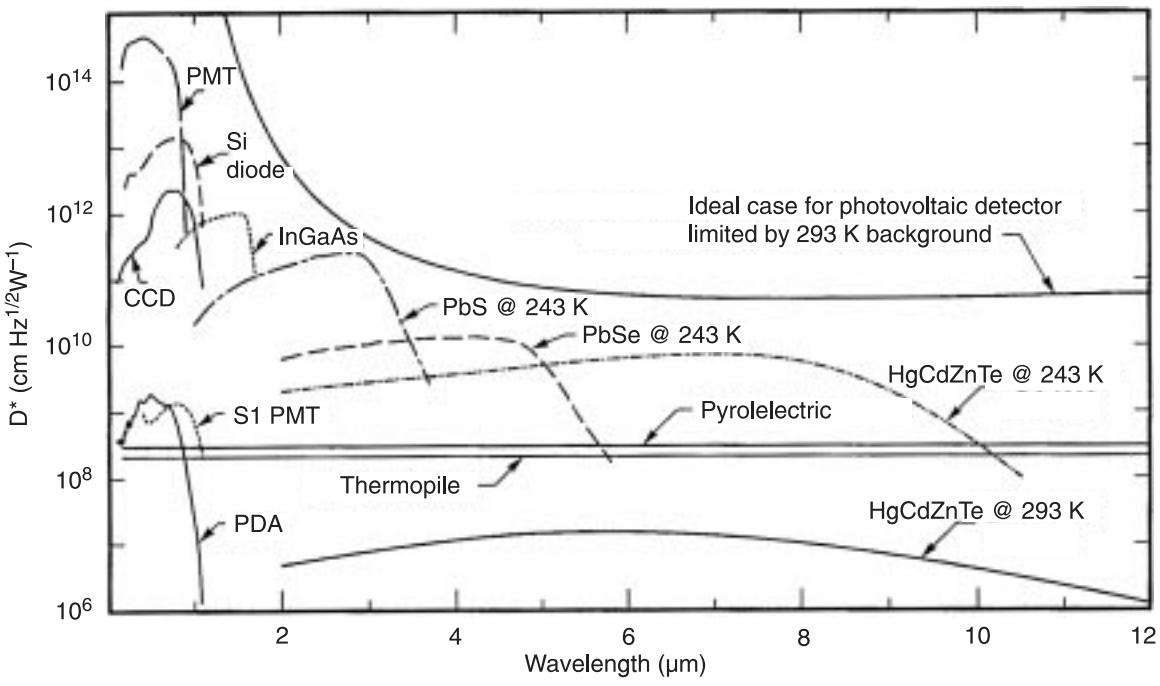

Fig. 1. Detectivity D^* versus wavelength for selected photodetectors.

$$D^* = (q\eta/h\nu)[(4kT/R_0A)]^{-1/2} = (q\eta/h\nu)(R_0A/4kT)^{1/2} \quad (3)$$
$$(\mathrm{cmHz}^{1/2}\mathrm{W}^{-1}),$$

where k is Boltzmann's constant and T is the absolute temperature. Note that the detectivity D^* is directly proportional to $(R_0A)^{1/2}$ when the detector is noise-limited. Thus, to develop very sensitive detectors it is essential that the detector noise sources be minimised so that R_0A is large. In the case of III-V nitrides, the extremely large density of dislocations represents a significant noise source. Therefore dislocation reduction should have a very positive effect on the detectivity of nitride photodiodes.

If the second term in the brackets of Eq. (2) above dominates, then the background signal determines D^*. In this case, the detectivity D^* is BLIP-limited and may be expressed as

$$D^*_{BLIP} = (q\eta/h\nu)\left[2q^2\eta\Phi_b\right]^{-1/2} = (1/h\nu)(\eta/2\Phi_b)^{1/2} \quad (4)$$
$$(\mathrm{cmHz}^{1/2}\mathrm{W}^{-1}).$$

The detectivity D^* may also be expressed in terms of the detector noise equivalent power NEP such that [12]

$$D^* = (A\Delta f^{1/2}/NEP) \quad (\mathrm{cmHz}^{1/2}\mathrm{W}^{-1}) \quad (5)$$

where A is the detector area and Δf is the detector bandwidth. The noise equivalent power NEP is the power that corresponds to the incident rms optical power required such that the detector signal-to-noise ratio is one in a bandwidth of 1 Hz.

3. Experimental details

3.1. Photodiode structures

Diode structures were prepared by MOVPE using a low-pressure, vertical-flow reactor that employs high speed substrate rotation during film growth. The photodiode structures were deposited onto double-side polished 50-mm diameter c-plane sapphire substrates. A thin AlN buffer layer was first deposited at 500–650°C to initiate growth; all subsequent layers were grown at 1050–1080°C.

A schematic of a representative photodiode structure employed in the present work, which is designed to respond to UV radiation in the range 320–365 nm, is shown in Fig. 2(a). As shown in the figure, the thin low temperature AlN nucleation layer is first deposited, followed by a ~1.0-μm thick n-type silicon doped $Al_{0.23}Ga_{0.77}N$ base layer. An undoped 0.2-μm thick GaN layer is then deposited, followed by a 0.5-μm thick p-type magnesium doped GaN layer to complete the p-i-n heterostructure. Note that this device structure is designed for through-the-substrate illumination. The photodiode structure shown in Fig. 2(a) responds to UV light in the wavelength band from about

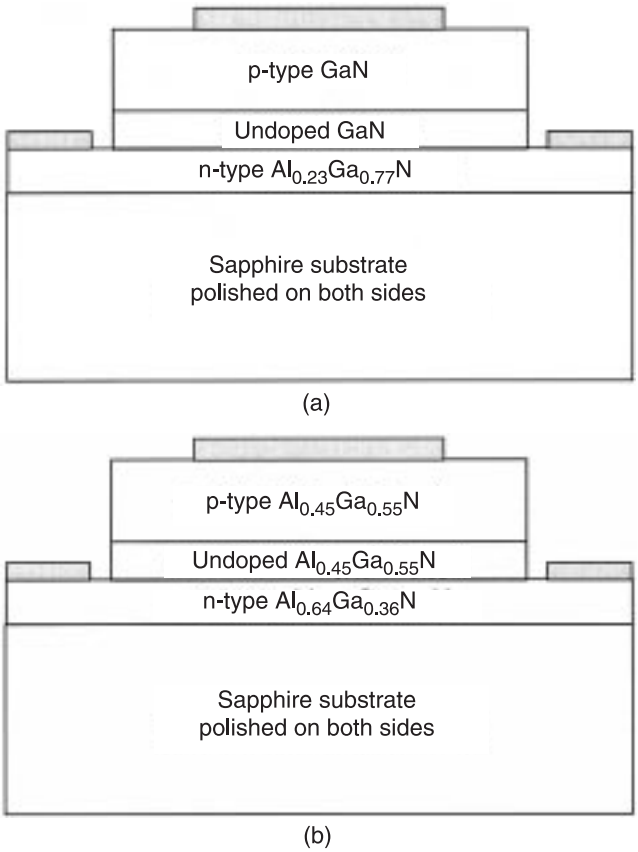

Fig. 2. Schematic representation of device structures used for (a) visible-blind photodiodes, and (b) solar-blind photodiodes.

320 nm to 365 nm. At wavelengths shorter than 320 nm, the incoming light is absorbed in the thick AlGaN base layer (~23% Al) and the junction is not illuminated. Likewise, the diode does not respond to wavelengths greater than 365 nm, since this corresponds to the optical absorption edge of GaN at 300 K.

Using the basic device structure shown in Fig. 2(a), it is possible to tailor the responsivity window of the UV detector by adjusting the aluminium mole fraction present in each of the three layers. Thus, it is possible to synthesise detectors that sense different UV spectral regions. For example, the diode structure shown in Fig. 2(b) is designed to sense UV light in the 240–285 nm 'solar blind' spectral region. In order to optimise the above photodiode structures, a series of samples were grown under various combinations of growth temperatures, growth rates, and gas flow rates. For example, for the solar-blind diode structure, the n-type $Al_{0.64}Ga_{0.36}N$:Si was first optimised. Capacitance-voltage (C-V), optical absorption, and cathodoluminescence (CL) measurements were employed in this optimisation procedure. The undoped $Al_{0.45}Ga_{0.55}N$ active layer and p-type magnesium doped $Al_{0.47}Ga_{0.53}N$:Mg top layer of the device structure were then optimised with the aid of optical absorption and cathodoluminescence measurements.

3.2. Device processing

All device processing was completed using standard semiconductor processing techniques which included photolithography using appropriately-designed masks, reactive ion etching to define mesa structures, and metallisations to provide ohmic contacts to the n-type and p-type layers of the devices. Boron trichloride (BCl_3) was employed in the reactive ion etching chamber using photolithographically defined Ni masks to etch the photodiode mesas. Etch rates of ~17.5 nm/s were obtained using BCl_3 flow rates of 35 sccm at a chamber pressure of 30 mTorr and an RF power level of 100 W. The discrete photodiodes used for responsivity and R_0A measurements employed 200×200 μm mesas. The 128×128 photodiode arrays employed 32×32 μm mesa diodes on a 38 μm pitch. The larger 320×256 photodiode arrays consisted of 24×24 μm mesa diodes on a 30 μm pitch. Ni/Au and Ti/Al metallisations, followed by an anneal at 600–700°C, were employed to obtain p-type and n-type ohmic contacts, respectively.

The UV photodiode arrays were hybridised to silicon readout integrated circuits (ROICs) using In bump bonds. Indigo Systems Corp. 9802 and 9809 ROICs were employed for hybridising the 128×128 and 320×256 photodiode arrays, respectively. In this flip-chip bonding procedure, photoresist was used to define 18 μm circular vias at all of the p-contact and n-contact points of the photodiode array, and at the corresponding metal pads of the Si ROIC. A dedicated UHV deposition system which employs MBE-type effusion cells was then used to precisely deposit a uniform array of In bumps of thickness 5–10 μm onto both the photodiode array and the Si ROIC. The photodiode array was then hybridised to the Si ROIC using an RD Automation model M8-G flip-chip aligner bonder. The hybridised focal plane array (FPA) was then cemented onto an 84-pin leadless chip carrier (LCC). Outputs from the ROIC were wire-bonded to the LCC using gold wires. The UV camera chip was then inserted into a matching 84 pin socket located on a circuit board in focal plane array evaluation and demonstration camera system obtained from SE-IR Corp. The SE-IR camera system employs a UV-compatible fused quartz focusing lens along with hardware and software for reading out, displaying and storing UV images from the 128×128 and 320×256 FPAs as single snap-shots, or as digital movies at selected frame rates under computer control.

3.3. Device testing

Spectral responsivity R_λ measurements were completed on selected photodiode samples. In these experiments, a xenon lamp was employed as a UV source and the UV illumination wavelengths were selected by a monochromator. The monochromator output was calibrated using a calibrated UV-enhanced Si photodiode. The spectral responsivity R_λ was then calculated from the measured photocurrent using Eq. (1).

The 300 K dynamic photodiode resistance at zero-bias R_0 was measured for selected devices using a shielded low-noise enclosure and shielded probe tips. These measurements were combined with the device area A to obtain the R_0A product – a well-known photodiode figure of merit. The R_0A product was then used to obtain an estimate of the noise-limited detector detectivity D^* using Eq. (3).

Alphanumeric and geometric objects were recorded with the 128×128 and 320×256 UV digital camera chips by using templates that were back-illuminated with a UV lamp, as shown in Fig. 3. For the visible-blind (300–365 nm) FPAs, templates were constructed using ink jet printer transparency sheets onto which were printed objects of interest, and a UV lamp producing 300–370 nm radiation was employed to back-illuminated these objects. UV images of an oxy acetylene torch and a TIG arc welder were also obtained by imaging these UV sources directly with the UV digital camera.

For the solar-blind (240–285 nm) FPAs, brass templates with milled-out alpha-numeric patterns were employed, and these were illuminated with the 253.6 nm output from a Hg(Ar) lamp.

Array statistics were investigated using the SE-IR FPA evaluation software, which could be used to output the signal voltages from each of the pixels in the hybridised array, or from a selected subset of pixels. For the 320×256 visible-blind arrays, the pixel dark noise current I_{DK} was first calculated from

$$I_{DK} = C(\Delta V/\Delta t) \text{ (A)}, \tag{6}$$

where C is the capacitance of the ROIC integration capacitor (13.3 μV/e), ΔV is the measured pixel noise voltage signal, and Δt is the integration time (16.54 ms). The noise equivalent power (NEP) was then calculated for each pixel of the hybridised array using [12]

$$NEP = I_{DK}/R_\lambda \text{ (W)}, \tag{7}$$

where R_λ is the spectral responsivity. Finally, the pixel detectivity D^* was estimated using Eq. (5), in which Δf = 60 Hz, and $A = (24\times10^{-4})^2 = 5.76\times10^{-6}$ cm^2.

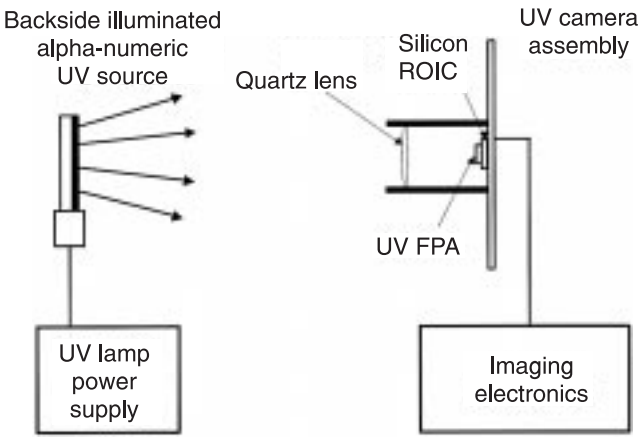

Fig. 3. Illustration of experimental setup employed for testing UV focal plane arrays.

To evaluate the hybridised FPAs under illumination, the arrays were subjected to a uniform UV illumination (300–370 nm) of moderate intensity, and the photocurrent I_{PH} from each pixel was calculated using Eq. (6), in which ΔV is the measured pixel photovoltage signal.

4. Results and discussion

4.1. Discrete UV photodiode characteristics

Figure 4 shows plots of the room temperature spectral responsivity R_λ versus wavelength for two selected UV photodiode samples. In Fig. 4(a), the responsivity for a visible-blind photodiode is shown. It is seen that the responsivity reaches its maximum value of 0.2 A/W at a wavelength of 358 nm. According to Eq. (1), this corresponds to an external quantum efficiency of 70%. Assuming the reflection losses at the air-sapphire, sapphire-AlGaN, and AlGaN-GaN interfaces is about 12% [5], one obtains an internal quantum efficiency of about 82% for this device. The responsivity remains fairly constant until about 320 nm and then begins to decrease rapidly as optical absorption occurs in the $Al_{0.2}Ga_{0.8}N$ base layer of the device. $R_0A = 1.5\times10^9\ \Omega\,cm^2$ and $D^* = 6.1\times10^{13}\ cmHz^{1/2}W^{-1}$ for this discrete photodiode. This D^* value, obtained at room temperature, is one of the largest D^* values ever obtained for any semiconductor photodetector operating at any temperature and at any wavelength. As illustrated by Fig. 1, this D^* value is approaching that of commerically available UV photomultiplier tubes (PMTs). Thus, with continued development, the nitride-based UV photodiodes may provide a solid state alternative to PMTs in the UV spectral region.

Figure 4(b) shows a responsivity spectrum obtained for a representative solar-blind UV photodiode at zero bias (photovoltaic mode). The solar-blind device exhibits a very narrow UV spectral responsivity band peaked at 265 nm, well within the 240–285 nm solar blind window, with a FWHM = 21 nm. The maximum responsivity R = 0.0952 A/W at 265 nm corresponds to an internal quantum efficiency of 53%. The responsivity falls off sharply at wavelengths greater than 285 nm since the device is transparent in this wavelength region. Likewise, the responsivity becomes very small at wavelengths shorter than 250 nm due to absorption in the n-type $Al_{0.64}Ga_{0.36}N$:Si base layer of the device. Thus, the AlGaN heterostructure that has been developed produces a narrow solar-blind responsivity band without the need for any external filters. $R_0A = 2.0\times10^9\ \Omega\ cm^2$ for this discrete solar-blind UV photodiode, corresponding to a detectivity $D^* = 3.3\times10^{13}\ cmHz^{1/2}W^{-1}$ at 265 nm.

4.2. 128×128 visible-blind focal plane arrays

UV imagery obtained using a 128×128 visible-blind focal plane array is illustrated in Figs. 5, 6 and 7. In Fig. 5, UV images of selected geometric shapes are shown. These images illustrate the high pixel yield (greater than 95%) that has been achieved for this type of UV digital imager.

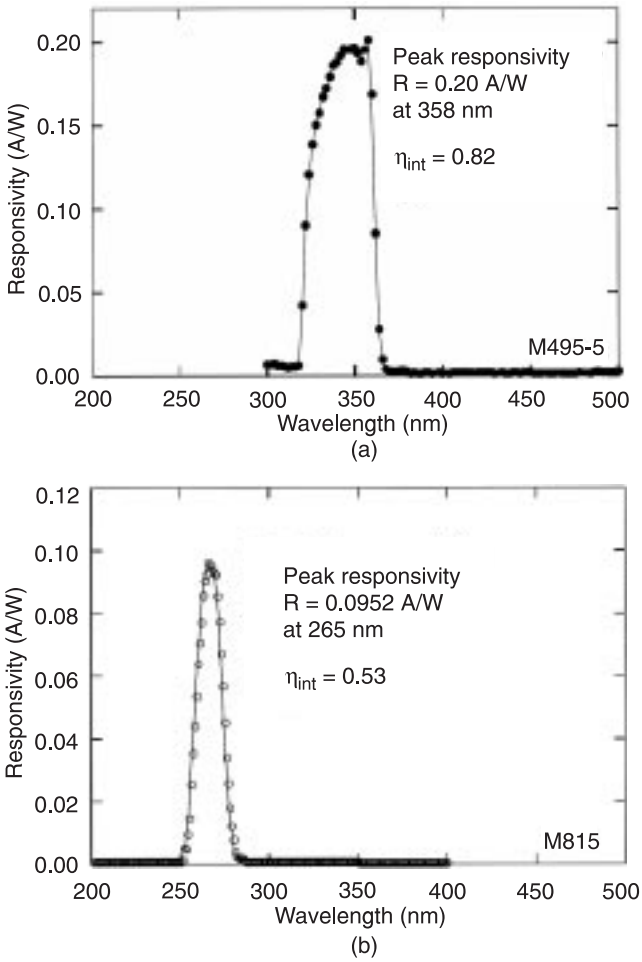

Fig. 4. Spectral responsivity versus wavelength for (a) visible-blind UV detector and (b) solar-blind UV detector.

Figure 6 shows both a visible image of a tungsten-inert-gas (TIG) arc welder and the corresponding UV emission (320–365 nm) from the arc welder that was obtained using the 128×128 FPA. In order to obtain the UV image shown, it was necessary to use a neutral density #4 filter in front of the UV camera to reduce the UV emission intensity from the arc welder and thus avoid pixel saturation. Figure 7 shows similar UV imagery (300–365 nm) obtained from an oxy-acetylene torch. It should be noted that all of the UV images were obtained at room temperature under standard room lighting. Note, however, that the 128×128 FPA is entirely blind to all visible radiation.

4.3. 320×256 visible-blind focal plane arrays

A selection of UV images obtained using a 320×256 visible-blind nitride focal plane array are shown in Figs. 8–12. In Fig. 8(a), a visible image of a standard television test pattern is shown. Below this image, in Fig. 8(b), is the UV image obtained from the corresponding template that was

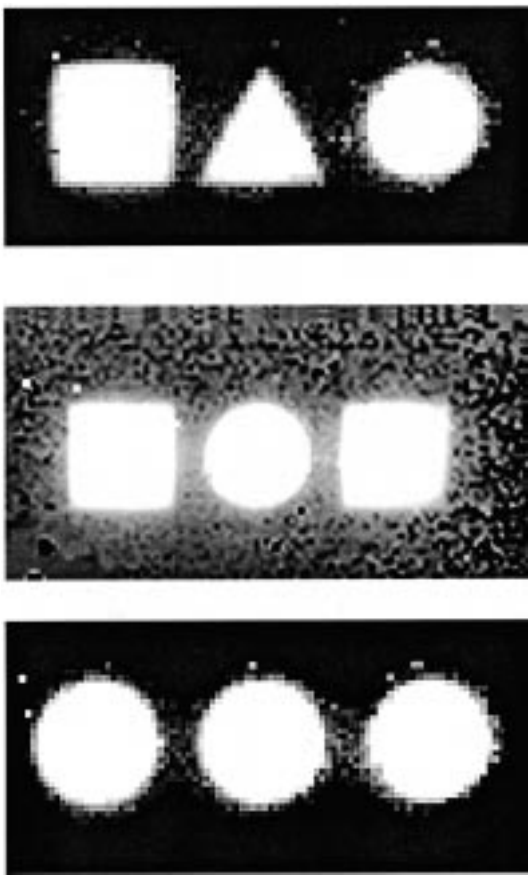

Fig. 5. UV digital images obtained using 128×128 visible-blind UV FPA.

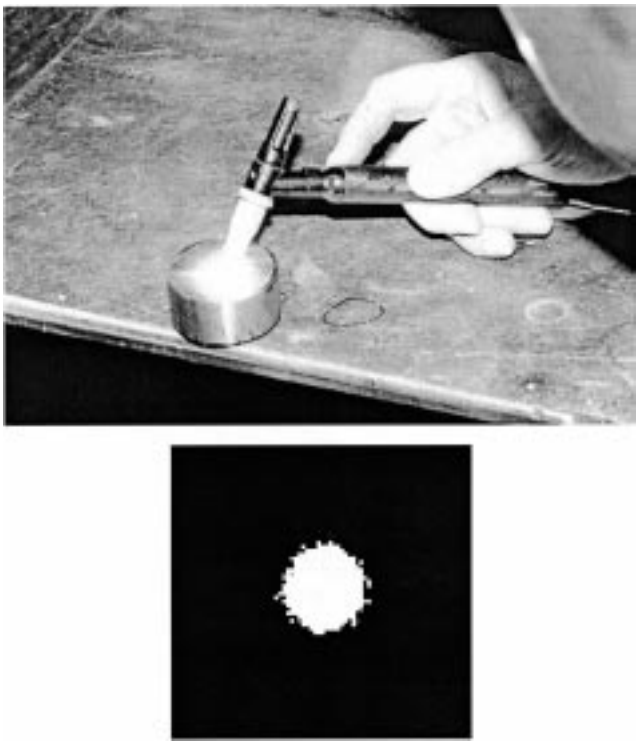

Fig. 6. Visible and UV images obtained for TIG arc welder.

Fig. 7. Visible and UV images obtained for oxy-acetylene torch.

back-illuminated with the UV source as described in Section 3.3 and imaged using the visible-blind 320×256 UV FPA. It is seen from the figure, that excellent detail is present in the UV image shown.

In Fig. 9(a), a visible image of a standard brightness/contrast test pattern is shown. The UV image of this test pattern is shown in Fig. 9(b). Again, excellent brightness and contrast ranges are present in the UV image shown.

In Fig. 10 (a), a visible image of the Engineering Graduate Research Centre on the North Carolina State University campus is shown. Below this, in Fig. 10(b), the corresponding UV image, obtained via the template technique described above, is shown. Note that excellent detail is present in the UV image.

Figure 11(a) shows a visible image of a person. Below this, in Fig. 11(b), the corresponding UV image obtained with the 320×256 visible-blind FPA is shown. Note the high percentage of active pixels in this UV image and the excellent brightness/contrast range exhibited in the image.

Figure 12(a) shows a visible image of a complex vertical line spectrum. This image is actually from a standard bar code, but could well represent a complex optical emission spectrum in the UV. This type of image was chosen to illustrate both the UV imagery and channel scan capabilities of the 320×256 UV FPA. In Fig. 12(b), the UV image of the bar code, obtained using the 320×256 visible-blind UV FPA, is illustrated. Note that the UV image shows excellent reproducibility of the various lines shown in the visible image. In Fig. 12(c), a channel scan from the 320×256

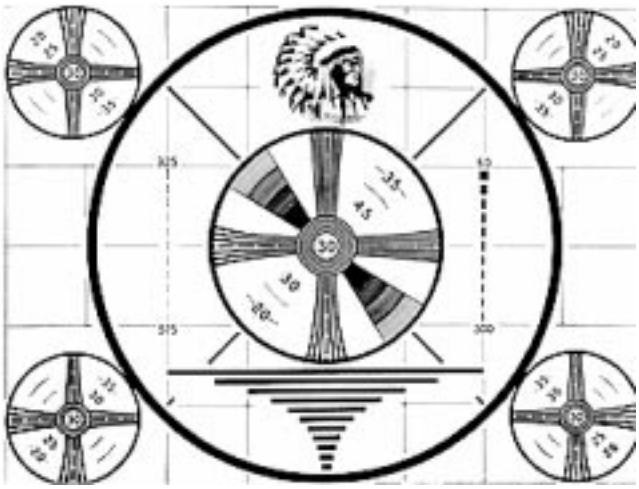

(a)

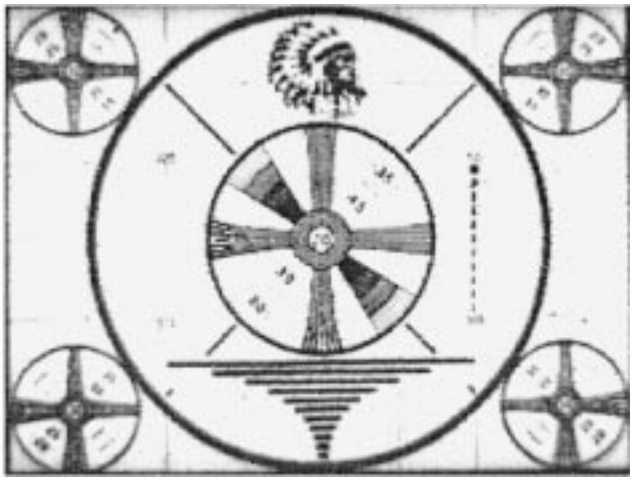

(b)

Fig. 8. Standard television test pattern: (a) visible image; (b) UV image.

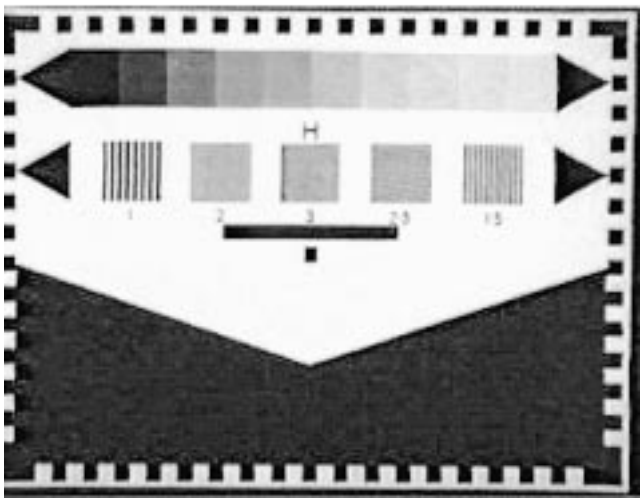

(a)

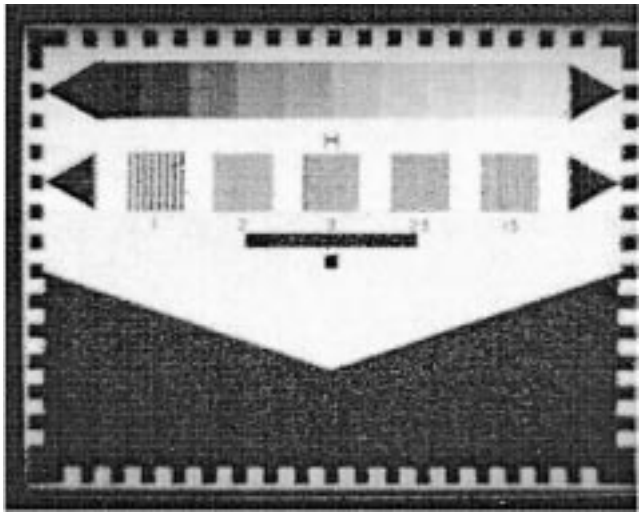

(b)

Fig. 9. Standard brightness/contrast test pattern: (a) visible image; (b) UV image.

UV FPA is shown. In this case, the total photocurrent from each of the 256 vertical pixels associated with each of the 320 horizontal channels has been summed under software control and displayed as a channel spectrum. This illustrates that the new UV FPAs may find use as a fast 320-channel solid-state UV detector array when used as the output detector for UV spectrometer, for example. The 300–365 nm UV wavelength region is particularly important for fluorescence spectroscopy for bioagents such as anthrax, or other biomaterials containing tryptophan.

4.4. 320×256 solar-blind focal plane arrays

Several solar-blind FPAs have also been successfully fabricated and tested. To date, however, only a portion of these arrays were found to be active imagers, due to the poorer quality of the high aluminium content materials that must be employed to produce solar-blind detectors and detector arrays. In addition, in order to obtain UV images from a solar-blind array it is necessary that a solar-blind UV source be employed. In the present study, solar-blind UV images were obtained by using brass templates with geometric cut-outs that were back-illuminated with the 253.6 nm line from a Hg(Ar) lamp and imaged with the UV FPAs. Figure 13 illustrates several solar-blind geometric images obtained using this technique. Note that the quality of the solar-blind imagery is not nearly as good as the images obtained using the 320×256 visible blind FPAs.

4.5. 320×256 visible-blind array characteristics

Histograms for the pixel distributions of the dark current noise I_{DK}, the photocurrent $I_{PH,}$, the noise equivalent power *NEP*, and the detectivity D^* were obtained for selected 320×256 visible-blind hybridised arrays using the SE-IR FPA evaluation software. Results of these studies are shown in Figs. 14 and 15 for a representative 320×256 visible-blind FPA. It should be noted that the Indigo 9809 ROIC employed is equipped with a capacitance-trans im-

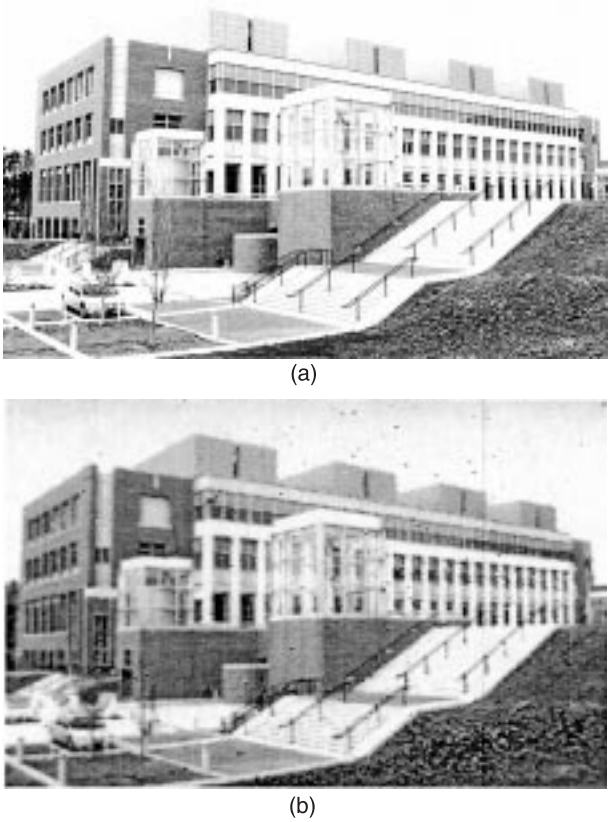

Fig. 10. Engineering Graduate Research Center on the North Carolina State University campus: (a) visible image; (b) UV image.

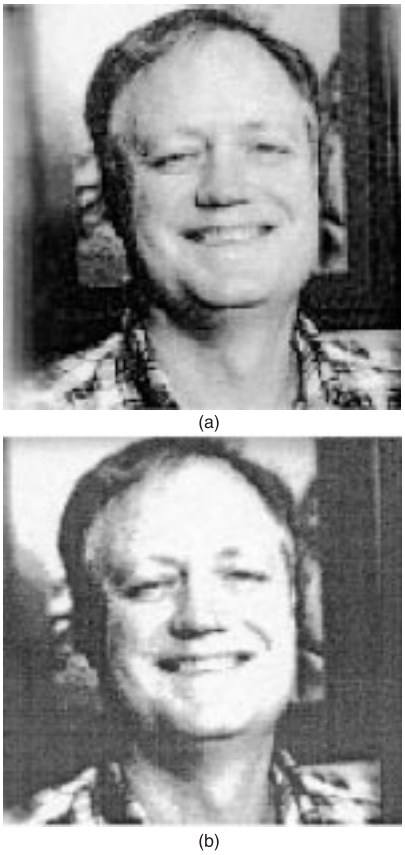

Fig. 11. Images of person: (a) visible image; (b) UV image.

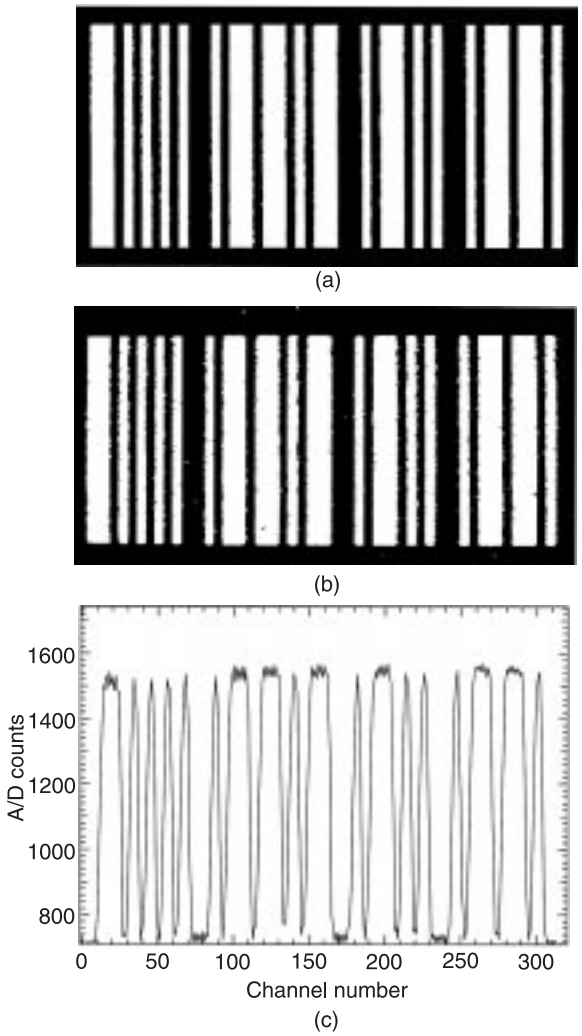

Fig. 12. Bar graph: (a) visible image; (b) UV image; (c) photocurrents from horizontal channel scan.

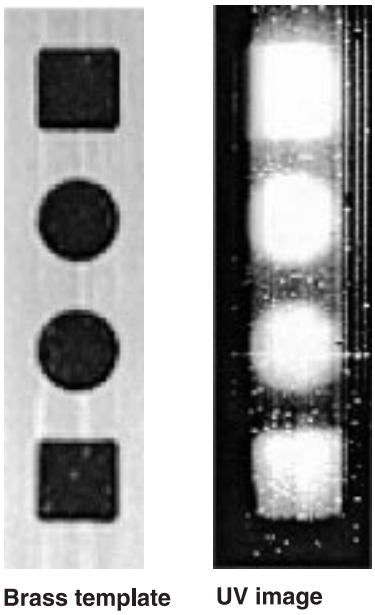

Fig. 13. Images of geometric objects using 320×245 solar-blind UV FPA.

pedance-amplifier (CTIA) input stage such as to produce very low noise. The hybridised FPA histograms reflect the combined noise characteristics of both the Si ROIC and the nitride photodiode array.

Figure 14(a) shows the distribution of dark noise currents. It is seen that a large majority of the FPA pixels exhibit very low dark currents in the range $3–7\times10^{-16}$ A. Under a moderate uniform UV illumination, the FPA shows excellent pixel photocurrent uniformity, peaked at about 2.26×10^{-12} A for the illumination intensity employed.

Using the data shown in Fig. 14(a), along with Eqs. (5) and (7), histograms for the *NEP* and *D** were obtained for selected 320×256 FPAs. Representative histograms are shown in Fig. 15. It is seen that the pixel noise equivalent power forms a tight distribution peaked at about 2×10^{-15} W. This corresponds to a distribution of detectivities peaked at about 1×10^{13} cmHz$^{1/2}$W^{-1}, as shown in Fig. 15(b).

These results emphasize the very low noise and very high sensitivity that the visible-blind nitride UV FPAs exhibit.

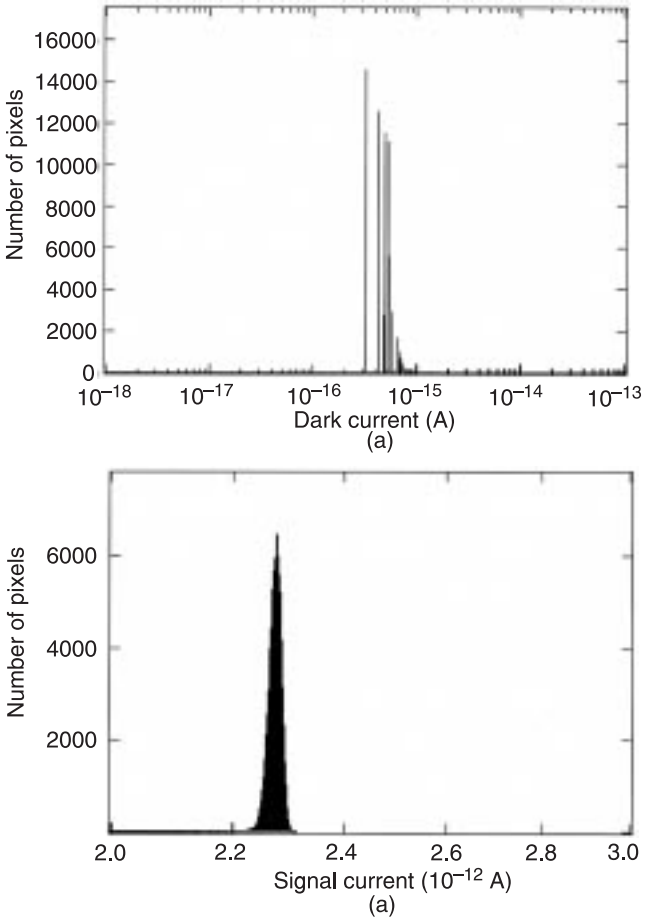

Fig. 14. 320×256 FPA histograms: (a) distribution of dark (noise) currents; (b) distribution of photocurrents.

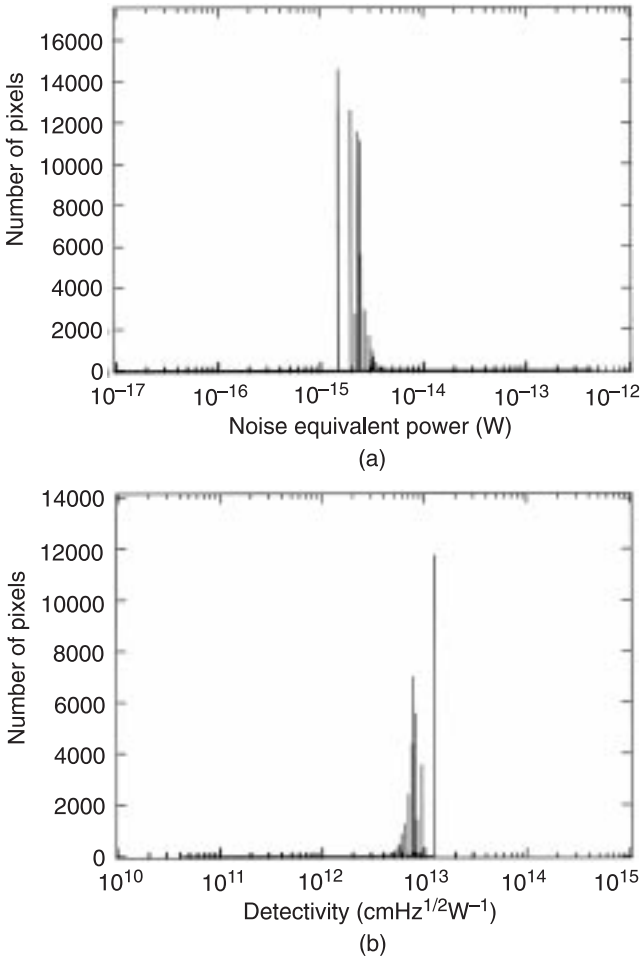

Fig. 15. 320×256 FPA histograms: (a) NEP distribution; (b) *D** distribution.

5. Conclusions

The successful development of both discrete UV photodiodes and large-format UV imaging arrays consisting of 128×128 and 320×256 AlGaN p-i-n photodiodes is reported. These devices exhibit very low noise and very high sensitivity to UV radiation. Excellent quality UV images have been obtained for both 128×128 and 320×256 large format hybridised FPAs. These new devices may find widespread usage in a number of applications that require sensitive UV detectors and UV imagers.

Acknowledgements

The work at NCSU is being supported by Defence Advanced Research Projects Agency grants DAAD 19-99-0010 and N00014-00-C-0407. Many former NCSU students contributed to this work including J.D. Brown, J. Muth, J. Boney, P. Srinivasan, and M.A.L. Johnson. T. Nohava and W. Yang of Honeywell Laboratories provided some of the MOVPE wafers used to process the samples. In addition, we wish to acknowledge the support of S. Petronio and J. Barton at Indigo Systems for their help with

the hybridisation of large focal plane arrays. Professor J.C. Campbell of the University of Texas at Austin gratuitously granted permission to use his photograph for the UV imagery demonstration of Fig. 11.

References

1. See, for example, IR digital cameras that are available from Indigo Systems (http://www.indigosystems.com).
2. C.E. Kolb, S.B. Ryali, and J.C. Wormhoudt, "The chemical physics of ultraviolet plume signatures", *Proc. SPIE* **932**, 2 (1988).
3. H. Morkoc, "GaN-based modulation-doped FETs and UV detectors", *Naval Research Reviews* **51(1)**, 26 (1999).
4. D.K. Wickenden, Z. Huang, D. Brent Mott, and P.K. Shu, "Development of gallium nitride photoconductive detectors", *Johns Hopkins APL Technical Digest* **18(2)**, 217 (1997).
5. W. Yang, T. Novova, S. Krishnankutty, R. Torreano, S. McPherson, and H. Marsh, "Back-illuminated GaN/AlGaN heterojunction photodiodes with high quantum efficiency and low noise", *Appl. Phys. Lett.* 73(8), 1086 (1998).
6. T. Huang, D.B. Mott, and A. La, "Development of 256×256 ultraviolet imaging arrays", *Proc. SPIE* **3765**, 254 (1999).
7. J.D. Brown, J. Matthews, S. Harney, J. Boney, J.F. Schetzina, J.D. Benson, K.V. Dang, T. Nohava, W. Yang, and S. Krishnankutty, "Visible-blind UV digital camera based on a 32×32 array of GaN/AlGaN p-i-n photodiodes", *MRS Internet J. Nitride Semicond. Res.* **4**, 9 (1999).
8. J.D. Brown, J. Matthews, S. Harney, J.C. Boney, J.F. Schetzina, J.D. Benson, K.V. Dang, T. Nohava, W. Yang, and S. Krishnankutty, "High-sensitivity visible-blind AlGaN photodiodes and photodiode arrays", *MRS Internet J. Nitride Semicond. Res.* **5S1**, W1.9 (2000).
9. J.D. Brown, J. Boney, J. Matthews, P. Srinivasan, J.F. Schetzina, T. Nohava, W. Yang, and S. Krishnankutty, "UV-specific (320–365 nm) digital camera based on a 128×128 focal plane array of GaN/AlGaN p-i-n photodiodes", *MRS Internet J. Nitride Semicond. Res.* **5**, 6 (2000).
10. D. Walker, V. Jumar, K. Mi, P. Kung, X.H. Zhang, and M. Razeghi, "Solar-blind AlGaN photodiodes with very low cutoff wavelength", *Appl. Phys. Lett.* **76**, 403 (2000).
11. E.L. Tarsa, P. Kozodoy, J. Ibbetson, and B.P. Keller, "Solar-blind AlGaN-based inverted heterostructure photodiodes", *Appl. Phys. Lett.* 77, 316 (2000).
12. S.L. Chuang, *Physics of Optoelectronic Devices*, Wiley, New York (1995).
13. *The Book of Photon Tools*, pp. 1–25, distributed by Oriel Corporation (http://www.oriel.com).

